RSC Advances

ROYAL SOCIETY OF CHEMISTRY

www.rsc.org/advances

Magnetoplasmons in simple hexagonal graphite

Rong-Bin Chen,[*a‡1] **Chih-Wei Chiu,**[*b‡2] **Ming-Fa Lin,**[c]

Received Xth XXXXXXXXXX 20XX, Accepted Xth XXXXXXXXX 20XX
First published on the web Xth XXXXXXXXXX 200X
DOI: 10.1039/b000000x

Magneto-electronic Coulomb excitations in simple hexagonal graphite (SHG) are studied within the random-phase approximation. They strongly depend on the direction, the magnitude of the transferred momentum **q**, and the magnetic field strength. The plasmon frequency dispersion in the perpendicular component q_z in the primitive unit cell and its parallel component $q_\parallel$ are very different from each other. The former shows only one prominent peak. The plasmon frequency increases with q_z, while the intensity of the plasmon peak exhibits the opposite behavior. The latter presents many plasmon peaks. Moreover, the threshold frequency of the loss spectrum for SHG is higher than that of monolayer graphene. As the field strength increases, the plasmon peaks are intensified. The group velocity for plasmon propagation along $\widehat{q}_z$ is typically positive for a fixed field strength. The q_z-dependence of the plasmon frequency is gradually reduced with an increased field strength. Graphite quite differs from graphen in magneto-electronic excitations, including the intensity, number and frequency of magnetoplasmons.

1 Introduction

Graphene layers have attracted a lot of studies recently due to the successful production by mechanical friction[1,2] and micromechanical cleavage.[3] Very strong sp^2 bonds in each graphene layer cause a threefold-coordinated planar structure with the remaining p_z orbital perpendicular to the plane. These special π electrons dominate the physical properties at low energy. The interlayer interactions owning to the van der Waals forces coupled the graphene layers.[4] Thus, the characteristics of the material have a strong dependence on the stacking-configuration,[5–7] layer numbers,[8–13] and the interlayer atomic interaction.[14–17] For an AA-stacked simple hexagonal graphite (SHG), the π bands are no longer symmetric to the π^* bands about Fermi level $E_F = 0$.[18] The overlap of the lowest conduction band (c) and the highest valence band (v) leads to a few free carriers, and thus such a system is considered a semimetal. However, the electronic excitations provide a reasonable explanation for the measured absorption spectra and loss spectra. In this work, we mainly study the low-frequency magneto-electronic Coulomb excitations in AA-stacked graphite, their dependence on the magnitude and the direction of the transferred momentum, and the magnetic field strength. A comparison with SHG in the absence of a magnetic field and monolayer graphene (MG) is also presented.

In the presence of a perpendicular magnetic field $B\widehat{z}$, the planar motions of electrons are effectively quantized to form dispersionless Landau levels (LLs). Thus, in bulk graphite, the planar electrons' motion turns into the Landau orbitals, while the motion along the field remains intact. The electronic bands of graphite are converted into one-dimensional ones, the so-called Landau subbands (LSs). The LSs of graphites exhibit many important features. Such as SHG possesses very strong k_z-dependent energy dispersions with a broad band width of about 1.4 eV (Fig. 1(a)), and each LS can be described by a simple relationship with k_z.[18,19] On the contrary, ABC-stacked rhombohedral graphite (RHG) presents weak k_z-dependent dispersions with a narrow band width ($\sim$10 meV).[20] The energy dispersion of AB-stacked Bernal graphite (BG) has a band width of $\sim$0.2 eV,[21,22] which lies between that of SHG and RHG, and two LSs cross E_F. The low-lying LSs are complex and cannot be easily described by k_z. The characteristics of LSs would be reflected in the magneto-optical spectra. For example, the magneto-optical absorption spectrum of SHG is dominated by intraband $(c \to c; v \to v)$ and interband $(v \to c)$ excitations which induce a multi-channel peak, several two-channel peaks, and many double-peak structures.[23] The prominent peaks of BG come from the interband excitations at both the K and H points. The peaks associated with the K point display double-peak structures.[21,24]

There are some theoretical studies on the magneto-electronic excitations in MG.[8,25,26] The previous results show that th single-particle excitations (SPE; e-h pairs) and collective excitations (plasmons) strongly depend on the transferred momentum, the magnetic-field strength, the temperature, and th

[a] *Center of General Studies, National Kaohsiung Marine University, Kaohsiung 811, Taiwan*
[b] *Department of Physics, National Kaohsiung Normal University, Kaohsiung 824, Taiwan*
[c] *Department of Physics, National Cheng Kung University, Tainan 701, Taiwan*
‡1 E-mail: rbchen@mail.nkmu.edu.tw
‡2 E-mail: giorgio@fonran.com.tw

doped free carrier density. These two kinds of excitations, which are caused by the Coulomb excitations from the occupied LLs to the unoccupied ones, can be clearly characterized by the special peak structures in the dielectric function and the energy loss function, respectively. The magnetoplasmons present the non-monotonous momentum-dependence, indicating the strong competition between the longitudinal Coulomb oscillation and the transverse magnetic quantization. Furthermore, the critical momentum of plasmon is determined by the Landau damping (the non-vanishing e-h pairs). The increasing temperature or free carrier density will induce new plasmon modes, but reduce the original plasmon intensities. Since the LSs have the strong k_z-dependent energy dispersions, SHG is expected to exhibit the feature-rich magneto-electronic excitation spectra.

The magneto-electronic properties are studied by means of the Peierls tight-binding model and band-like matrix numerical techniques,[23,24,27] through which the electronic structures at realistic magnetic fields can be solved. In the random-phase approximation (RPA), the complete structure of the dielectric function (ε) was determined. SPE and collective excitations can be presented as the imaginary part of the dielectric function ε_2 and the loss function, respectively. The calculations of the electron-energy-loss spectroscopy (EELS) show that the π plasmon is characterized by the prominent peak. The π plasmon originates from the interband excitations, and its cause will be studied. The electronic Coulomb excitations, strongly depend on both the magnitude and direction of the transferred momentum $\mathbf{q}$. The stacking-order could further affect the anisotropy which is reflected in the main features of the dielectric function and thereby the loss function. As a result of this anisotropy, the magnetoplasmon dispersions with respect to $\mathbf{q}$ are remarkably different between MG and AA-stacked graphite. Moreover, the group velocities of the magnetoplasmons in the long wavelength limit are typically positive as q is increased.

2 Peierls tight-binding model and dielectric function

For a simple hexagonal graphite, the geometric structure is formed by periodically stacked monolayer graphene along the z-direction. All the honeycomb structures in SHG have the same projections on the x-y plane. The C-C bond length is $b = 1.42$ Å, and the interlayer distance is $I_c = 3.50$ Å.[28] The primitive unit cell includes two atoms A and B; the intralayer and interlayer atomic interactions α_i were obtained from the study of Charlier.[15] When SHG is subjected to a $B\hat{z}$, the path integral of the vector potential induces a periodical Peierls phase.[29] The phase term of the associated period is inversely proportional to the magnetic flux ($\Phi = 3\sqrt{3}b^2B/2$) through a hexagon. To satisfy the integrity of the primitive cell, the ratio $R_B = \Phi_0/\Phi$ ($\Phi_0 = hc/e$, flux quantum) has to be a positive integer. As a result, the extended rectangular unit cell has $4R_B$ carbon atoms. The π-electronic Hamiltonian built from the $4R_B$ tight-binding functions is a $4R_B \times 4R_B$ Hermitian matrix. To solve this huge matrix problem, one can convert the Hamiltonian matrix into a band-like form by rearranging the tight-binding functions.[23,24,27] Both eigenvalue $E^{c,v}$and eigenfunction $\Psi^{c,v}$are efficiently obtained, even for a small magnetic field. The superscripts c and v, respectively, represent the conduction and valence bands.

The main features of the magneto-electronic properties are directly manifested in the electronic Coulomb excitations. Electronic excitations are characterized by the transferred momentum $\mathbf{q}$= $(q sin\theta, 0, q\cos\theta) = (q_{\|}, 0, q_{\perp})$ and the excitation energy ω; here, θ is the angle between $\mathbf{q}$ and the z-axis. At arbitrary temperature T, the dielectric function calculated for bulk graphite in the RPA[30,31] is

$$\varepsilon(q,\theta,\omega) = \varepsilon_0 - v_q \sum_{h',h} \int_{1st\ BZ} 2\,\frac{d^3\mathbf{k}}{(2\pi)^3} \left| \left\langle \mathbf{k}+\mathbf{q}; h' \left| e^{i\mathbf{q}\cdot\mathbf{r}} \right| \mathbf{k}; h \right\rangle \right|^2 \times \frac{f(E_{h'}(\mathbf{k}+\mathbf{q})) - f(E_h(\mathbf{k}))}{E_{h'}(\mathbf{k}+\mathbf{q}) - E_h(\mathbf{k}) - (\omega + i\Gamma)}, \quad (1)$$

where $\mathbf{k}$ and $\mathbf{q}$ are three-dimensional wave vectors, $v_q = 4\pi e^2/q^2$ is the bare Coulomb interactions, and $\varepsilon_0 = 2.4$ is the background dielectric constant for graphite.[32] $E_{h'}(\mathbf{k}+\mathbf{q})$ and $E_h(\mathbf{k})$ are the state energies of the final and initial states. The labels h(h′) denote the conduction or valence bands. Γ is the broadening parameter due to various deexcitation mechanisms and $f(E_h(\mathbf{k}))$ is the Fermi-Dirac distribution function. In demonstrating the anisotropy of the dispersion relation of the π-plasmons, it is considered that the inelastic scattering only involves $q_{\|}$ along the hexagonal plane in the Brillouin zone, i.e., k_z is conserved and $q_z = 0$.

3 Results and discussion

A magnetic field causes the cyclotron motion in the x-y plane; therefore, the LSs are formed along $\widehat{k_z}$ for SHG, as shown in Fig.1(a). Each LS possesses two band-edge states K ($k_z = 0$) and H($k_z = \pi/I_c$), respectively. The LS energies decrease as k_z gradually grows. The main features of the wave functions could be utilized to define the quantum number of the LSs. The wave functions are composed of the subenvelope function (ϕ_n) of the harmonic oscillator, as shown in Fig.1(b) for $k_z = 1$ (π/I_c). The number of zero points (n) of (ϕ_n) is utilized to define the quantum number (n^c or n^v) of each LS. For the sake of convenience, the LS with quantum number n^c(n^v) is represented as LS^{n^c} (LS^{n^v}). The wave function is associated with th

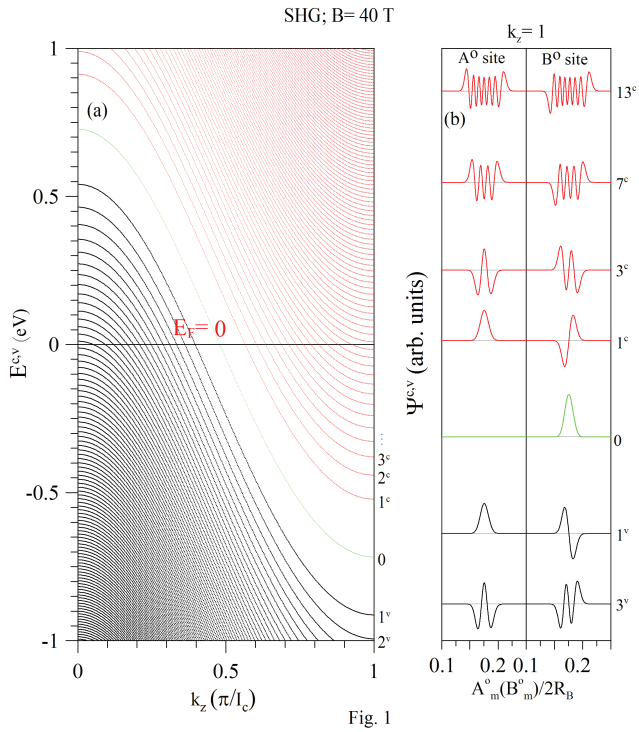

Fig. 1

Fig. 1 (a) The Landau subbands at $B = 40$ T, where $n^{c,v}$'s are the quantum numbers. (b) The related wave functions associated with the Landau subbands at $k_z = 1$, A^o and B^o represent the A and B sublattices with odd indices, respectively.

odd index B^o (A^o) sublattice of the $LS^{n^{c,v}=n}$ is ϕ_n (ϕ_{n-1}). The numbers of zero points of ϕ_n's corresponding to the B^o sublattice are chosen as the quantumn numbers of the LSs. The conduction (valence) LSs with small n^c (n^v) values crossing the E_F imply that parts of these LSs are occupied states and the others are unoccupied states. Such a feature might cause the intraband and interband transitions in the Coulomb excitations.

The calculated q-dependent SPE and collective plasmon modes due to the screened Coulomb interaction can be well described by the behavior of the imaginary part ε_2 and the real part ε_1 of the dielectric function. The special structures in ε_2 and ε_1 satisfy the Kramers-Kronig relation because of the Coulomb response. The features display a peak structure in ε_2, and a peak and dip structure along the zero points in ε_1. As $q_\parallel = 0$ and $B = 40$ T, the SPE spectrum ε_2 only shows one peak which originates from intraband excitations $(c \to c; v \to v)$, as shown in Fig. 2(a) by the blue curve. In the absence of a magnetic field, ε_2 presents also only one prominent peak resulting from the intraband excitation (circles in Fig.2(a)). Such excitations come from the band states along the $K - H$ line.[33] The dielectric functions in the $B = 0$ and $B \neq 0$ cases are very similar to each other. The main reason is that a magnetic field causes the cyclotron motion in the x-y plane and $q_\parallel = 0$ ($k_\parallel$ conserved). Furthermore, increasing q_z reduces the peak intensity that occurs at higher frequencies, which involve the lower LSs intraband and interband excitations $(v \to c)$ (Fig. 2(b)).

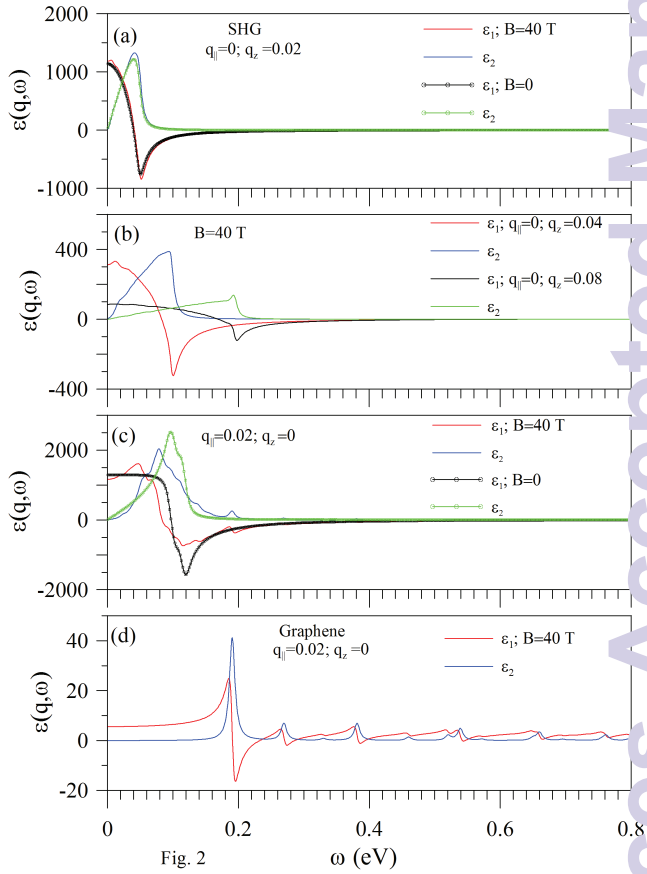

Fig. 2

Fig. 2 The real (ε_1) and imaginary (ε_2) parts of the dielectric function of SHG for different values of $q_\parallel$ and q_z. (a) $q_\parallel = 0$ and $q_z = 0.02$, (b) $q_\parallel = 0$ and $q_z = 0.04$; $q_\parallel = 0$ and $q_z = 0.08$, (c) $q_\parallel = 0.02$ and $q_z = 0$. (d) The dielectric function of MG at $q_\parallel = 0.02$ and $q_z = 0$. For comparison, at $B = 0$ the dielectric function of SHG is also plotted. The unit of $q_\parallel$ (q_z) is $\AA^{-1}$, here and elsewhere in this paper.

The electronic excitations are significantly changed by th direction of **q**; that is, they exhibit the highly anisotropic behavior. As $q_z = 0$ (k_z conserved), the SPE spectrum is dominated by the intraband and interband excitations. For $B = 40$ T

the first prominent peak of ε_2 is associated with the intraband excitations, as shown in Fig. 2(c) by the blue solid curve. For the frequency range $\omega > 0.1$ eV, the SPE spectrum relates to the interband excitations. For $B = 0$, SHG presents only one prominent peak in ε_2 (circles in Fig. 2(c)), which is associated with the intraband and interband excitations. In short, the special structures of ε exhibit the blue shift and the weaker intensity in the increase of momentum, being determined by the LS energy dispersions and the q-dependent Coulomb interactions . The dielectric function might have more special structures for larger $q_\parallel$.

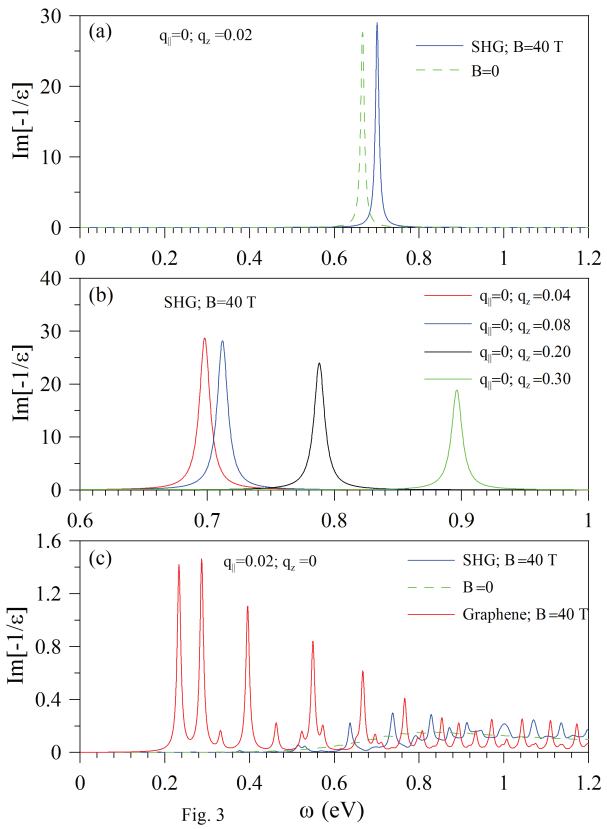

Fig. 3

Fig. 3 (a) At $B = 40$ T, the energy loss function of SHG for different values of $q_\parallel$ and q_z. Panels (a) and (b) are at $q_\parallel = 0$ and various q_z's, and (c) $q_\parallel = 0.02$ and $q_z = 0$. The loss spectrum of MG at $q_\parallel = 0.02$ and $q_z = 0$ is plotted in panel (c). At $B = 0$, the energy loss function of SHG is illustrated for comparison.

To comprehend the effects in the absence of stacking on the ε, the spectra of MG are shown in Fig. 2(d). In the dielectric function of MG, each Landau level (LL) transition channel produces a symmetric peak in ε_2 and a pair of asymmetric peaks along the zero points in ε_1. MG does not exhibit any intraband excitation since the valence (conduction) LLs are occupied (unoccupied). In short, in the range of $\omega < 0.1$ eV, $q_\parallel = 0$ and a small q_z, the dielectric functions of SHG are alike in the $B \neq 0$ and $B = 0$ cases. The absorption peaks (ε_2) all originate from the intraband excitations. However, under the condition that $q_z = 0$, $B \neq 0$, a small $q_\parallel$, and the frequency range $\omega > 0.1$ eV, the dielectric function of SHG is related to the interband excitations, and similar to that of MG.

The energy loss function, defined as $\mathrm{Im}[-1/\varepsilon(q,\omega)]$, is useful for comprehending the collective excitations and the directly measured excitation spectra. SHG presents only one peak in Fig. 3(a), for $q_\parallel = 0$ and $q_z = 0.02$ $\AA^{-1}$ at $B = 40$ T. The unit of $q_\parallel$ (q_z) is $\AA^{-1}$, here and elsewhere in this paper. This peak is regarded as the collective excitations only arising from the interband excitations. For $\omega < 0.6$ eV, ε_1 and ε_2 are quite large and hardly contribute to the energy loss function. Furthermore, the temperature only has an effect on the composite threshold peak which is caused by the intraband excitations.[2] As a result, the temperature effects are negligible in the collective excitations. The higher plasmon intensity corresponds to a zero point in ε_1 and a small value in ε_2. At $q_\parallel = 0$, the plasmon peaks are very prominent. The plasmon peaks diminish their intensity and exhibit a blue shift as q_z increases (Fig. 3(b)). The loss spectra are very sensitive to a change in the direction of the $\mathbf{q}$. At $q_\parallel = 0.02$ and $q_z = 0$, the spectrum of SHG is shown in Fig. 3(c) by the solid blue curve. The plasmon peaks originating from the higher LS transitions have smaller heights mainly because of the reduced wave function overlap and the larger Landau damping out of the denser LS distribution. On the other hand, as the interlayer atomic interactions and the k_z dependence are neglected, SHG can be considered as a MG for calculations. The loss spectrum of MG exhibits a lower threshold frequency and a higher intensity than that of SHG. These results indicate that SHG is subject to very strong Landau damping for a large value of ε_2 in the low-frequency region (Fig. 2(c)). This reflects the fact that the LSs of SHG provide an effective k_z-range, whereas LLs of MG do not, as the weak van der Waals interlayer interactions[4] induce many electrons and holes in the SHG configuration. At $B = 0$ and $q_z = 0$, no prominent peak is shown in the low-frequency region. This clearly indicates that a uniform magnetic field can change the electron density of states and consequently enhances the low-lying plasmon excitations. Apparently, the important differences between SHG and MG lie in the intensity, number and frequency of plasmon peaks in the energy energy loss function. They come from the dimension-dependent Coulomb interactions and magnetic energy subbands.

The influence of the magnetic field strength on the loss spectrum deserves a closer examination. As Fig. 4 shows, at $q_\parallel = 0$ one prominent peak is retained in the low-frequency range. When the field strength decreases, the loss spectrum presents red-shifted frequencies and a weaker intensity. This reflect

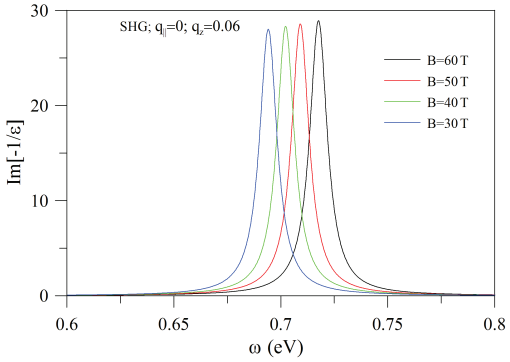

Fig. 4

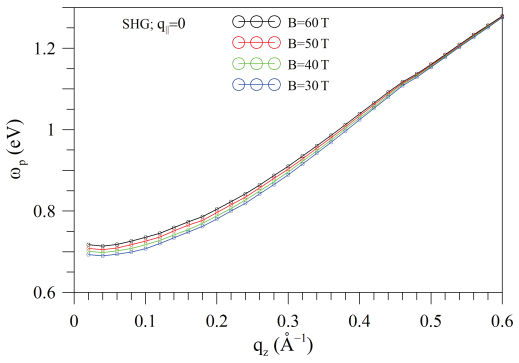

Fig. 5

Fig. 4 The energy loss functions at $q_{\|} = 0$ and $q_z = 0.06$ for different magnetic field strengths.

Fig. 5 Plot of magnetoplasmon frequency as a function of q_z and $q_{\|} = 0$ for certain field strength. The plasmon dispersion depends on the chosen magnetic field.

the fact that the state degeneracy and effective k_z-range of the LSs are proportional to B. The variation of plasmon frequency with q_z is shown in Fig. 5 for selected field strengths. The strong dispersion relation of the plasmon frequency ω_p with q_z means that the plasmon oscillation behaves as a propagating wave with wavelength $2\pi/q_z$ and group velocity $\nabla_{q_z}\omega_p(q_z)$. The group velocity of plasmon propagation along $\widehat{q_z}$ is typically positive for a fixed B. Moreover, ω_p is finite when $q_z \to 0$ and is within the region of optical scattering spectroscopies. Therefore, the magnetoplasmon apparently belongs to an optical plasmon.[34] The q_z significantly affects the plasmon frequency even at larger values. Moreover, the q_z-dependence of ω_p is gradually reduced with increasing field strength. This result directly reflects the LSs of SHG characteristics.

4 Conclusion

We have employed the Peierls tight-binding model to calculate the electron energy bands of SHG in a perpendicular magnetic field $B\widehat{z}$. In the calculations, the intralayer and interlayer atomic interactions, the magnetic fields and the Coulomb interactions are taken into account simultaneously. The similar method can also be used to investigate the magneto-electronic Coulomb excitations in AB- and ABC-stacked graphites. By means of rearranging the base functions, the eigenvalues and the wave functions can be efficiently obtained at weaker field strength. With these results, we calculated the longitudinal dielectric function within the RPA. The dielectric function strongly depends on the direction, the magnitude of the transferred momentum $\mathbf{q}$, and the magnetic field strength. In the range of $\omega < 0.1$ eV, the q_z-dependent dielectric functions of SHG are alike in the $B \neq 0$ and $B = 0$ cases; the absorption peaks all originate from the intraband excitations. However, for the range $\omega > 0.1$ eV ($B \neq 0$), the $q_{\|}$-dependent dielectric functions of SHG are related to the interband excitations. The plasmon dispersion in the q_z-dependence and $q_{\|}$-dependence cases are very different from each other. The former only exhibits a single prominent peak whose plasmon frequency ω_p increases with q_z, while its intensity diminishes. In the latter case, many peaks are present. Moreover, the loss spectrum of monolayer graphene exhibits a lower threshold frequency and a higher intensity than that of SHG. As the field strength increases, the plasmon peaks of the energy loss function are intensified. The group velocity for plasmon propagation along $\widehat{q_z}$ is typically positive for a fixed B. Furthermore, the q_z-dependence of ω_p is gradually reduced

with increasing field strength. There exist certain important differences between SHG and MG, such as the strength, number, and frequency of magnetoplasmon. Electron-energy-loss spectroscopy or magneto-optical spectroscopy could be utilized to verify the predicted plasmons.

Acknowledgements

This work is supported in part by the NSC, under Grant No. NSC 102-2112-M-006-007-MY3.

References

1 J. S. Bunch, Y. Yaish, M. Brink, K. Bolotin and P. L. McEuen, *Nano Lett.*, 2005, **5**, 287.

2 C. Berger, Z. Song, T. Li, X. Li, A. Y. Ogbazghi, R. Feng, Z. Dai, A. N. Marchenkov, E. H. Conrad, P. N. First and W. A. de Heer, *J. Phys. Chem. B*, 2004, **108**, 19912.

3 K. S. Novoselov, A. K. Geim, S. V. Morozov, D. Jiang, Y. Zhang, S. V. Dubonos, I. V. Grigorieva and A. A. Firsov, *Science*, 2004, **306**, 666.

4 D. D. L. Chung, *J. Mater. Sci.*, 2002, **37**, 1475.

5 K. F. Mak, J. Shan and T. F. Heinz, *Phys. Rev. Lett.*, 2010, **104**, 176404.

6 Y. Liu, W. S. Lew, S. Goolaup, H. F. Liew, S. K. Wong and T. Zhou, *ACS Nano*, 2011, **5**, 5490.

7 M. Koshino, *New J. Phys.*, 2013, **15**, 015010.

8 O. L. Berman, G. Gumbs and Y. E. Lozovik, *Phys. Rev. B*, 2008 **78**, 085401.

9 Z. S. Wu, W. Ren, L. Gao, B. Liu, C. Jiang and H. M. Cheng, *Carbon*, 2009, **47**, 493.

10 Y. Hao, Y. Wang, L. Wang, Z. Ni, Z. Wang, R. Wang, C. K. Koo, Z. Shen and J. T. L. Thong, *Small*, 2010, **6**, 195.

11 M. V. Katkov, V. I. Sysoev, A. V. Gusel'nikov, I. P. Asanov, L. G. Bulusheva and A. V. Okotrub, *Phys. Chem. Chem. Phys.*, 2015, **17**, 444.

12 B. Partoens and F. M. Peeters, *Phys. Rev. B*, 2006, **74**, 075404.

13 K. S. Kumar, S. Pittala, S. Sanyadanam and P. Paik, *RSC Adv.*, 2015, **5**, 14768.

14 L. Samuelson, I. P. Batra and C. Roetti, *Solid State Commun.*, 1980, **33**, 817.

15 J.-C. Charlier, J.-P. Michenaud and X. Gonze, *Phys. Rev. B*, 1992, **46**, 4531.

16 X. Zhang and M. Zhao, *RSC Adv.*, 2015, **5**, 9875.

17 M. Kocman, M. Pykal and P. Jurečka , *Phys. Chem. Chem. Phys.*, 2014, **16**, 3144.

18 R. B. Chen and Y. H. Chiu, *J. Nanosci. Nanotechnol.*, 2012, **12**, 2557.

19 B. A. Bernevig, T. L. Hughes, S. Raghu and D. P. Arovas, *Phys. Rev. Lett.*, 2007, **99**, 146804.

20 C. H. Ho, C. P. Chang, W. P. Su and M. F. Lin, *New J. Phys.*, 2013, **15**, 053032.

21 K.-C. Chuang, A. M. R. Baker and R. J. Nicholas, *Phys. Rev. B*, 2009, **80**, 161410(R).

22 Y. H. Ho, Y. H. Chiu, W. P. Su and M. F. Lin, *Appl. Phys. Lett.*, 2011, **99**, 011914.

23 R. B. Chen, Y. H. Chiu and M. F. Lin, *Carbon*, 2013, **54**, 268.

24 Y. H. Ho, J. Wang, Y. H. Chiu, M. F. Lin and W. P. Su, *Phys. Rev. B*, 2011, **83**, 121201(R).

25 R. Roldán, J.-N. Fuchs and M. O. Goerbig, *Phys. Rev. B*, 2009, **80**, 085408.

26 J.-Y. Wu, S.-C. Chen, O. Roslyak, G. Gumbs and M. F. Lin, *ACS Nano*, 2011, **5**, 1026.

27 Y. H. Lai, J. H. Ho, C. P. Chang and M. F. Lin, *Phys. Rev. B*, 2008, **77**, 085426.

28 J. K. Lee, S. C. Lee, J. P. Ahn, S. C. Kim, J. I. B. Wilson and P. John, *J. Chem. Phys.*, 2008, **129**, 234709.

29 R. Saito, G. Dresselhaus and M. S. Dresselhaus , *Physical Properties of Charbon Nanotubes*; Imperial College Press: London, 1998. p. 98.

30 H. Ehrenreich and M. H. Cohen, *Phys. Rev.*, 1959, **115**, 786.

31 K. W.-K. Shung, *Phys. Rev. B*, 1986, **34**, 979.

32 E. A. Taft and H. R. Philipp, *Phys. Rev.*, 1965, **138**, A197.

33 F. L. Shyu and M. F. Lin, *J. Phys. Soc. Jpn.*, 2001, **70**, 897.

34 C. Kittel, *Introduction to Solid State Physics, 8th ed.*; John Wiley & Sons, Inc., 2005, p. 96.

FIGURE CAPTIONS

Fig. 1. (a) The Landau subbands at $B = 40$ T, where $n^{c,v}$'s are the quantum numbers. (b) The related wave functions associated with the Landau subbands at $k_z = 1$, A^o and B^o represent the A and B sublattices with odd indices, respectively.

Fig. 2. The real (ε_1) and imaginary (ε_2) parts of the dielectric function of SHG for different values of $q_\parallel$ and q_z. (a) $q_\parallel = 0$ and $q_z = 0.02$, (b) $q_\parallel = 0$ and $q_z = 0.04$; $q_\parallel = 0$ and $q_z = 0.08$, (c) $q_\parallel = 0.02$ and $q_z = 0$. (d) The dielectric function of MG at $q_\parallel = 0.02$ and $q_z = 0$. For comparison, at $B = 0$ the dielectric function of SHG is also plotted. The unit of $q_\parallel$ (q_z) is $\mathring{A}^{-1}$, here and elsewhere in this paper.

Fig. 3. (a) At $B = 40$ T, the energy loss function of SHG for different values of $q_\parallel$ and q_z. Panels (a) and (b) are at $q_\parallel = 0$ and various q_z's, and (c) $q_\parallel = 0.02$ and $q_z = 0$. The loss spectrum of MG at $q_\parallel = 0.02$ and $q_z = 0$ is plotted in panel (c). At $B = 0$, the energy loss function of SHG is illustrated for comparison.

Fig. 4. The energy loss functions at $q_\parallel = 0$ and $q_z = 0.06$ for different magnetic field strengths.

Fig. 5. Plot of magnetoplasmon frequency as a function of q_z and $q_\parallel = 0$ for certain field strength. The plasmon dispersion depends on the chosen magnetic field.